

X-RAY RADIATION FROM THE MILLISECOND PULSAR J0437–4715

V. E. ZAVLIN¹, G. G. PAVLOV², D. SANWAL², R. N. MANCHESTER³, J. TRÜMPER¹, J. P. HALPERN⁴, AND W. BECKER¹

ABSTRACT

We report on spectral and timing observations of the nearest millisecond pulsar J0437–4715 with the *Chandra* X-ray Observatory. The pulsar spectrum, detected up to 7 keV, cannot be described by a simple one-component model. We suggest that it consists of two components, a nonthermal power-law spectrum generated in the pulsar magnetosphere, with a photon index $\gamma \approx 2$, and a thermal spectrum emitted by heated polar caps, with a temperature decreasing outwards from 2 MK to 0.5 MK. The lack of spectral features in the thermal component suggests that the neutron star surface is covered by a hydrogen (or helium) atmosphere. The timing analysis shows one X-ray pulse per period, with a pulsed fraction of about 40% and the peak at the same pulse phase as the radio peak. No synchrotron pulsar-wind nebula is seen in X-rays.

Subject headings: stars: neutron — pulsars: individual (PSR J0437–4715) — X-rays: stars

1. X-RAYS FROM MILLISECOND PULSARS: THERMAL VERSUS NONTHERMAL

Millisecond (recycled) radio pulsars are distinguished from ordinary pulsars by their very short and stable periods, $P \lesssim 10$ ms, $\dot{P} \sim 10^{-21} - 10^{-19}$ s s⁻¹. It is generally accepted that they are very old objects, with spin-down ages $\tau = P/2\dot{P} \sim 10^9 - 10^{10}$ yr and low surface magnetic fields $B \propto (P\dot{P})^{1/2} \sim 10^8 - 10^{10}$ G (e.g., Taylor, Manchester, & Lyne 1993). Similar to ordinary pulsars, a millisecond pulsar can emit nonthermal X-rays from its magnetosphere, with a hard power-law spectrum and sharp pulsations. In addition to this nonthermal radiation, thermal X-rays can be emitted from the neutron star (NS) surface, provided the surface is hot enough. According to the models of NS thermal evolution (albeit rather uncertain at these old ages), recycled pulsars are too cold (surface temperature $T \lesssim 0.1$ MK — see, e. g., Tsuruta 1998) to be detectable in X-rays. However, their polar caps can be heated up to X-ray temperatures by relativistic particles impinging onto the magnetic poles from the acceleration zones in the magnetosphere. The radio pulsar models (e.g., Cheng & Ruderman 1980; Arons 1981; Michel 1991; Beskin, Gurevich, & Istomin 1993) predict polar cap radii $R_{pc} \sim (2\pi R^3/Pc)^{1/2}$ (where $R \approx 10$ km is the NS radius), i.e., $R_{pc} \sim 1-5$ km for millisecond pulsars, although different models predict quite different polar cap temperatures, in the range of 1–10 MK. Detection of the polar cap thermal radiation would allow one to discriminate between various models of radio pulsars, study the properties of NS surface layers, and constrain the NS mass-to-radius ratio (Pavlov & Zavlin 1997; Zavlin & Pavlov 1998 [ZP98]). However, just as in the case of ordinary pulsars, this radiation is detectable only if it is not buried under stronger nonthermal radiation. The current theoretical models are not elaborate enough to predict in which (if any) of millisecond pulsars the thermal component can be brighter than the nonthermal one (in particular, both the thermal and nonthermal luminosities are expected to increase with spin-down energy loss \dot{E} , perhaps with different rates). Therefore, we have to rely upon the analysis of X-ray observations to distinguish the thermal and nonthermal components.

The X-ray observatories *ROSAT*, *ASCA*, and *BeppoSAX* have detected 11 millisecond pulsars (nearly 1/3 of all X-ray-detected rotation-powered pulsars — see Becker & Pavlov 2001 for a recent review). Five of these pulsars are identified in X-rays only by positional coincidence with the radio pulsars and, due to the low number of recorded counts, provide only crude flux estimates. The radiation from 3 pulsars — B1821–24 (Saito et al. 1997), B1937+21 (Takahashi et al. 2001), and J0218+4232 (Mineo et al. 2000) — is clearly nonthermal: their power-law spectra, detected with *ASCA* and *BeppoSAX* up to energies of 5–10 keV, are very hard, with photon indices $\gamma \sim 1$, and their pulse profiles show sharp peaks. Interestingly, these 3 pulsars are characterized by particularly large \dot{E} values, $\dot{E} = (2-20) \times 10^{35}$ erg s⁻¹, and their magnetic fields at the light cylinder, $B_{lc} = B(R/R_c)^3 \sim 10^6$ G, are close to that of the Crab pulsar. The case for the other 3 pulsars — J0437–4715 (Becker & Trümper 1993, 1999 [BT93, BT99]; ZP98), J2124–3358 (BT99), and J0030+0451 (Becker et al. 2000) — is less certain. These pulsars show broad peaks of X-ray pulsations, but it does not necessarily mean that their radiation is thermal because broad peaks can be produced by nonthermal emission at some viewing angles. High-quality spectra have been recorded for the brightest of these pulsars, J0437–4715, but their interpretation has been controversial — e.g., ZP98 suggest that the radiation detected with *ROSAT* and *EUVE* can be interpreted as thermal radiation from hot polar caps, whereas BT99 argue that the radiation is nonthermal (see §2). To resolve this controversy, the pulsar needed to be observed at energies above the soft *ROSAT* and *EUVE* bands ($E \gtrsim 2$ keV), and with high spatial resolution to avoid contamination of the pulsar emission by a nearby AGN which compromised the *ASCA* and *BeppoSAX* data.

The *Chandra* X-ray Observatory provides both the superb spatial resolution and high throughput at higher energies, together with timing capability. In this paper we present the results of our observations of PSR J0437–4715 with *Chandra*. We start from a summary of the previous results on PSR J0437–4715 in §2. The spectral and timing analyses of the *Chandra* data are presented in §3 and §4. Implication of the results are

¹ Max-Planck-Institut für Extraterrestrische Physik, D-85740 Garching, Germany; zavlin@mpe.mpg.de

² The Pennsylvania State University, 525 Davey Lab, University Park, PA 16802, USA; pavlov@astro.psu.edu

³ Australia Telescope National Facility, CSIRO, P. O. Box 76, Epping, NSW 1710, Australia

⁴ Columbia University, 520 W. 120th Street, Mail Code 5230, New York, NY 10027, USA

discussed in §5.

2. PREVIOUS X-RAY OBSERVATIONS OF PSR J0437–4715

At a distance $d = 139 \pm 3$ pc (van Straten et al. 2001), PSR J0437–4715 is the nearest and brightest X-ray millisecond pulsar known at both radio and X-ray wavelengths. It was discovered by Johnston et al. (1993) during the Parkes Southern radio pulsar survey. It has a spin period $P = 5.76$ ms, and, after correcting the observed period derivative for the kinematic term due to its large proper motion, a characteristic age $\tau \simeq 4.9$ Gyr, magnetic field $B \sim 3 \times 10^8$ G, and rotation energy loss rate $\dot{E} \sim 3.8 \times 10^{33}$ erg s⁻¹. It is in a 5.74 d binary orbit with a white dwarf companion of a low mass $M \simeq 0.2M_{\odot}$. Optical observations in H $_{\alpha}$ have revealed a bow-shock pulsar-wind nebula (PWN), caused by the supersonic motion of the pulsar through the interstellar medium, with the bow-shock apex at about 10'' south-east of the pulsar, in the direction of the pulsar's proper motion (Bell, Bailes, & Bessell 1993; Bell et al. 1995).

PSR J0437–4715 was the first millisecond pulsar detected in X-rays — BT93 observed it with the ROSAT Position Sensitive Proportional Counter (PSPC) in 1992 and discovered X-ray pulsations with a single broad pulse and a pulsed fraction $f_p \sim 30\%$ in the 0.1–2.4 keV energy range. They also found, and Halpern, Martin, & Marshall (1996; HMM96 hereafter) later confirmed, that f_p apparently increases with photon energy E and reaches about 50% at $E = 0.6–1.1$ keV. However, BT99 found no energy dependence of f_p from the PSPC observation of 1994. On the other hand, ZP98 analyzed the same data and claimed that the energy dependence of the pulse profile is statistically significant.

The pulsar spectrum is incompatible with a simple blackbody (BB) model even in the narrow PSPC band (BT93), but it can be fitted with a power-law (PL) model, with a photon index $\gamma = 2.2–2.5$ (BT93; HMM96; ZP98; BT99), indicating that the soft X-ray radiation might be nonthermal. However, the probable energy dependence of the pulsed fraction makes this interpretation questionable. In addition, the combined analysis of the PSPC and EUVE Deep Survey Instrument (DSI) data show that the PL fit is only marginally acceptable (HMM96; ZP98).

BT93 suggested that the pulsar spectrum consists of two components — in addition to a PL ($\gamma \approx 2.9$), representing magnetospheric emission, there is a BB component with $T_{\text{bb}} \sim 1.7$ MK emitted from a small area of 0.05 km², implying the existence of polar cap(s) on the NS surface. An alternative two-component model was explored by ZP98. They suggest that the temperature distribution in a polar cap should be nonuniform because the heat, released by decelerating magnetospheric particles in subphotospheric layers, propagates along the surface out from the small polar area where the energy is deposited, which results in a larger heated area with the temperature decreasing outwards. Applying the hydrogen NS atmosphere models of Zavlin, Pavlov, & Shibano (1996), ZP98 show that the entire soft X-ray spectrum and the pulse profiles detected with ROSAT and EUVE can be interpreted as thermal emission from two opposite polar caps where the temperature drops from $T_{\text{core}} = 1–2$ MK in a central cap (“core”) of radius $R_{\text{core}} = 0.2–0.5$ km to $T_{\text{rim}} = 0.3–0.5$ MK in the annulus (“rim”) with an outer radius $R_{\text{rim}} = 2–5$ km. The bolometric luminosity of the polar caps⁵, $L_{\text{bol}} = (2–3) \times 10^{30}$ erg s⁻¹, is consistent with

the prediction of the slot-gap model of radio pulsars developed by Arons (1981). The hydrogen column density towards the pulsar, $n_{\text{H},20} = n_{\text{H}}/(10^{20} \text{ cm}^{-2}) = 0.1–0.3$, obtained by ZP98, is consistent with the properties of the interstellar medium inferred from observations of other objects in the vicinity of the pulsar.

The ROSAT energy band, 0.1–2.4 keV, is too soft to discriminate between different two-component models — e.g., BT99 have shown that equally good fits of the ROSAT PSPC spectrum can be obtained with a two-component BB+BB model or a broken PL. The pulsar has been observed at higher energies with ASCA. Kawai, Tamura, & Saito (1998) report that the ASCA spectrum is more consistent with a BB model with $T_{\text{bb}} \approx 3$ MK than with a PL model. However, because of poor spatial resolution of ASCA, the pulsar spectrum was heavily contaminated by the radiation from a neighboring Seyfert galaxy, that hampered the spectral analysis. Therefore, to investigate the pulsar spectrum at higher energies and measure its pulse profile with high accuracy, we proposed to observe PSR J0437–4715 with Chandra. The results of the spectral, timing, and spatial analyses are presented below.

3. ACIS OBSERVATION AND SPECTRAL ANALYSIS

PSR J0437–4715 was observed with the Advanced CCD Imaging Spectrometer (ACIS; Garmire et al. 1992; Bautz et al. 1998) on 2000 May 29–30, with a 25.7 ks effective exposure. It was imaged on the back-illuminated chip S3 of the ACIS spectroscopic array. To mitigate the pile-up effect⁶, the pulsar was offset by 3.9 from the optical axis and observed using a 1/8 subarray, with a 0.4 s frame time. We extracted source-plus-background counts from a 5''-radius circle centered on the pulsar image, which includes about 98% of pulsar counts. To measure the background, we extracted counts from several regions at distances of at least 10'' from the pulsar, where the pulsar contribution is negligible. The background, 0.020 counts ks⁻¹ arcsec⁻², is rather uniform throughout the observed 8' × 1' sky area — in particular, we see no structures which could be interpreted as a PWN associated with the bow shock observed in H $_{\alpha}$. The source count rate is 306 ± 4 counts ks⁻¹ (0.12 counts per frame), for the standard grades 02346, in the 0.2–7.0 keV range (where the source prevails over the background).

To examine the effect of pile-up on the pulsar spectrum, we extracted the count-rate spectra from a 1''-radius circle centered at the pulsar (which contains 56% of source counts) and from an annulus with 1'' and 5'' radii. We compared the spectral shapes using a χ^2 test and found them to be the same with a probability of 92%–95% (depending on binning chosen). Since the annulus spectrum should not be affected by pile-up, we conclude that the effect of pile-up on the whole pulsar spectrum is negligible.

To search for possible spectral features in the ACIS spectrum, we used a method applied by Pavlov et al. (2001) to the dispersed X-ray spectrum of the Vela pulsar, obtained with the Chandra Low Energy Transmission Grating. We first binned the original detector channels of a 5 eV width in bins of an 80 eV width (comparable with the intrinsic detector resolution of ~ 100 eV). Then, we combined 4–5 sequential binned channels in groups of 320–400 eV widths to estimate the deviation in

⁵The values of polar cap radii and luminosities given in ZP98 should be multiplied by $\pi^{1/2}$ and π , respectively, because they used an erroneous normalization factor. This error does not affect their qualitative conclusions.

⁶See Chandra Proposers' Observatory Guide (POG); <http://asc.harvard.edu/udocs/docs/docs.html>

the number of source counts in each binned channel of a given group from the mean value in the group. The maximum deviation does not exceed a 1.8σ level, which allows us to conclude that the ACIS spectrum of PSR J0437–4715 reveals no significant spectral features. For further analysis, we binned the pulsar spectrum in 75 energy bins in the 0.2–7.0 keV range. For fitting the ACIS data, we used CCD responses generated with the CIAO 2.1 software and CALDB 2.7 calibration files.

To investigate as broad energy range as possible, we analyzed the ACIS spectrum together with the ROSAT PSPC spectra observed on 1992 September 20–21 (5.9 ks exposure) and 1994 July 2–6 (9.9 ks exposure). (A detailed description of the PSPC data and their analysis can be found in ZP98.) Our attempts to simultaneously fit the ACIS and PSPC spectra immediately showed that they disagree with each other at energies below 0.6 keV — models which fit the ACIS and PSPC spectra at $E > 0.6$ keV are well above the observed ACIS data points at lower energies (particularly in a 0.3–0.5 keV range). We have encountered the same problem with the Vela pulsar (Pavlov et al. 2001) and PSR 1055–52 (Sanwal et al. 2000) — the ACIS and PSPC spectra of these pulsars are in good agreement only if we discard ACIS events below $\simeq 0.6$ keV. This inconsistency is apparently associated with errors in the ACIS response at low energies, so we have to use the ACIS data only in the 0.6–7.0 keV range (63% of the source counts in 50 energy bins).

3.1. Single power law fit

Fitting the separate ACIS spectrum in the 0.6–7 keV range with a PL model yields a best-fit photon index $\gamma = 4.1$ (min $\chi^2_\nu = 61.17/47 = 1.30$), drastically different from that obtained for the PSPC spectrum ($\gamma = 2.4$). Not surprisingly, a single PL does not fit these spectra together (min $\chi^2_\nu = 366.8/96 = 3.82$), clearly indicating that more components are needed to get a satisfactory combined fit.

3.2. Power law plus single-temperature polar caps

It has been shown by ZP98 that even the narrow-band PSPC spectrum cannot be interpreted in terms of a single-temperature polar cap radiation — there is always an excess of observed counts over the model spectrum at higher energies, even for the hydrogen-atmosphere model that provides the hardest spectrum.

3.2.1. Hydrogen polar caps

To explore the possibility that the observed X-ray emission consists of thermal (polar cap) and nonthermal (magnetospheric) components, we start with a two-component model: PL plus two polar caps covered with hydrogen or helium⁷. We assume the gravitational redshift parameter $g_r \equiv (1 - 2GM/Rc^2)^{1/2} = 0.769$, which corresponds to the NS radius $R = 10$ km at $M = 1.4M_\odot$. To model the polar cap component, we should specify some values for ζ , the angle between the line of sight and rotation axis, and α , the angle between the magnetic and rotation axes. Measuring these angles from the swing of the radio polarization position angle at the pulse center is difficult for this pulsar because of the complex position angle

variations, apparently including polarization mode transitions (Navarro et al. 1997). However, it is reasonable to assume that the rotation axis of the pulsar is close the orbital momentum axis whose inclination angle, $\approx 43^\circ$, was determined by van Straten et al. (2001). On the other hand, the radio pulse morphology and polarization strongly suggest that the magnetic inclination α is very close to ζ , probably the difference does not exceed 2° . We choose $\zeta = \alpha = 45^\circ$ for our models of polar cap radiation. We have checked that variation of the angles by $\pm 10^\circ$ around these values makes no appreciable effect on the spectral parameters, and changes of the inferred radii of the polar caps do not exceed 15%.

This model provides an acceptable fit to the PSPC and ACIS data (see Fig. 1, left panels), with a minimum $\chi^2_\nu = 1.25$ (94 d.o.f) and best-fit parameters $n_{H,20} = 0.6 \pm 0.2$, $T_{pc} = 1.80 \pm 0.05$ MK, $R_{pc} = 0.15 \pm 0.02$ km (at $d = 140$ pc), and $\gamma = 2.8 \pm 0.1$ (the uncertainties here and below are given at a 68% level; the polar cap parameters are given as measured at the NS surface; the gravitational effects are taken into account to calculate the model spectra as seen by a distant observer — see Zavlin, Shibano, & Pavlov 1995). The bolometric luminosity of two polar caps is $L_{bol} = (0.9 \pm 0.2) \times 10^{30}$ erg s⁻¹ $\sim 0.2 \times 10^{-3}\dot{E}$, and the luminosity of the nonthermal component in the 0.1–10 keV range is $L_X = (3.1 \pm 0.4) \times 10^{30}$ erg s⁻¹ $\sim 0.8 \times 10^{-3}\dot{E}$. The thermal component prevails in the 0.6–2.7 keV band; the PL component, dominating at higher and lower energies, determines the estimated value of n_H and gives the main contribution to the EUVE DSI flux. Comparison with the EUVE DSI data shows that this model is only marginally acceptable, similar to the case of the single PL fit to the PSPC spectrum, described by HMM96 and ZP98. Also, the n_H values allowed by the fit to the DSI, PSPC and ACIS data still exceed the values $n_{H,20} = 0.1 - 0.3$ derived from independent measurements of the hydrogen column density towards objects in the vicinity of PSR J0437–4715 (see ZP98).

3.2.2. Blackbody polar caps

If we assume a standard blackbody model for the polar cap radiation, we obtain qualitatively similar results, with a higher temperature of the thermal component, $T_{bb} \simeq 2.9$ MK, and a much smaller radius of emitting area, $R_{bb} \simeq 0.04$ km. Spectral fits with the simplified blackbody model consistently produce higher temperatures and smaller sizes because X-ray spectra emerging from light-element atmospheres are harder than blackbody spectra (Zavlin et al. 1996).

3.2.3. Iron polar caps

Although the pulsar spectral fits are very comfortable with featureless models, it is worthwhile to check a hypothesis that the surface layers of polar caps are comprised of heavier chemical elements, e. g., iron. Using NS iron atmosphere models (Rajagopal & Romani 1996; Zavlin et al. 1996⁸) for the thermal (polar cap) component, we found that the single PSPC spectrum fits well with a power law plus iron atmosphere model, whereas the ACIS data of much better spectral resolution are inconsistent with this model, particularly around the (redshifted) L and K absorption features in the iron atmosphere spectrum

⁷The difference between the hydrogen and helium spectral models is very small in the X-ray range, at the temperatures of interest.

⁸The iron atmosphere spectra presented by Zavlin et al. (1996) were computed with an error in interpolating the opacity tables. We are grateful to R. Romani who brought our attention to this issue. The error has been corrected in the models used in this paper. An example of a corrected model spectrum has been presented by Pavlov & Zavlin (2000).

(at energies of 0.85 keV and 4.9 keV for $g_r = 0.769$ — see right panels in Fig. 1). Varying the gravitational redshift shifts the feature energies in the model spectrum, but the features remain too strong to be consistent with the smooth observed spectrum at any allowed values of g_r .

3.3. Power law plus polar caps with nonuniform temperature

ZP98 showed that a polar cap model with a nonuniform temperature distribution along the cap’s surface fits the PSPC spectrum without invoking a nonthermal component. They suggested a two-step approximation for the polar cap temperature distribution, a hot “core” plus a colder “rim” (see §2 and left panels of Fig. 2). Applying this model to the ACIS data shows that the observed spectrum significantly exceeds the model at $E > 2$ keV (the upper limit of the PSPC energy range) and obviously requires one more component. A natural choice for the additional component is a PL. Adding the nonthermal component greatly improves the fit (right panels in Fig. 2) reducing χ^2_ν from 2.39 to 1.13. This model has seven fitting parameters, some of them are strongly correlated (ZP98). The correlation is particularly strong between n_H and R_{rim} . Since the best-fit values of the hydrogen column density are well consistent with the values $n_{\text{H},20} = 0.1 - 0.3$ obtained from the independent estimates, we chose to fix the column density to weaken the correlations between the other six fitting parameters. For $n_{\text{H},20} = 0.2$, we obtain $T_{\text{core}} = 2.1^{+0.2}_{-0.3}$ MK, $T_{\text{rim}} = 0.54^{+0.06}_{-0.10}$ MK, $R_{\text{core}} = 0.12^{+0.04}_{-0.02}$ km, $R_{\text{rim}} = 2.0^{+0.3}_{-0.2}$ km, and $\gamma = 2.2^{+0.3}_{-0.6}$. Varying the hydrogen column density within the $n_{\text{H},20} = 0.1 - 0.3$ range results in a minor change ($< 7\%$) in the values of R_{rim} and R_{core} (at the other parameters fixed). In this model the bolometric luminosity of two polar caps is $L_{\text{bol}} = (2.3 \pm 0.6) \times 10^{30} \text{ erg s}^{-1} \sim 0.6 \times 10^{-3} \dot{E}$, and the PL luminosity in the 0.1–10 keV range is $L_X = (0.7 \pm 0.3) \times 10^{30} \text{ erg s}^{-1} \sim 0.2 \times 10^{-3} \dot{E}$. Note that this model is in good agreement with the EUVE DSI data.

One may assume that the additional component to fit the hard tail of the ACIS spectrum is also a thermal one, instead of the PL. However, this thermal component has to be of a very high temperature, $T \sim 12 - 15$ MK, emitted from a very small area of 1–2 m radius. Although we are not aware of reliable calculations of temperature distributions around pulsar’s magnetic poles, we believe that such a steep gradient in the temperature distribution is unlikely.

3.4. Broken power law

Although the power-law plus polar-cap models fit the PSPC+ACIS spectra satisfactorily, one cannot rule out *a priori* that the (purely nonthermal) pulsar spectrum bends down somewhere in the X-ray band, which might be caused, e.g., by a deficit of high-energy electrons in the pulsar’s magnetosphere. To test this hypothesis, we applied a broken PL model to the PSPC and ACIS spectra and obtained an acceptable fit ($\chi^2_\nu = 1.31$) with $n_{\text{H},20} = 0.3^{+0.5}_{-0.2}$ and photon indices $\gamma_1 = 2.0 \pm 0.2$ and $\gamma_2 = 3.6 \pm 0.1$, below and above the break energy $E_b = 1.1 \pm 0.1$ keV, respectively. However, the EUVE DSI flux calculated with the best-fit parameters exceeds the observed DSI flux by about 3σ (if one adopts a 15% systematic uncertainty in the DSI flux). Including the DSI data in the combined analysis shows that the broken PL model can be accepted at the same low-confidence level as in the case of the PL plus single-temperature polar cap model fit, and it requires $n_{\text{H},20} > 0.5$.

⁹See: <http://asc.harvard.edu/ciao2.2/test/ahelp/axbary.html>

Broken PL spectra have been observed from young ordinary pulsars, but with a much higher break energy, in the GeV range. However, no breaks have been observed in the spectra of other millisecond pulsars, and the (single) PL slopes measured in the three millisecond pulsars with certainly nonthermal radiation are more gradual than the slopes of the broken PL components in PSR J0437–4715. Therefore, although we cannot completely reject the broken PL interpretation, we consider it less plausible than the power-law plus thermal polar-cap model.

4. HRC OBSERVATIONS AND TIMING ANALYSIS

PSR J0437–4715 was observed with the imaging array of the High Resolution Camera (HRC-I; Murray et al. 1997) on 2000 February 13, with a 18.9 ks effective exposure. The pulsar was detected with a source count rate of 174 ± 4 counts ks^{-1} (estimated in a $3''$ -radius circle centered at the pulsar’s position). The image of the pulsar and its surroundings is shown in Figure 3. The surface brightness of the background in the pulsar vicinity, 0.015 counts $\text{ks}^{-1} \text{ arcsec}^{-2}$ is so low that its contribution is negligible in the source aperture, and the count rate error is determined solely by the source photon statistics. Figure 4 shows the extracted radial distribution of the (energy-integrated) encircled source count fraction. The distribution is well consistent with that expected for a point source.

Our attempts to detect pulsations in these data failed. The reason of this failure was found later — a wiring error in the HRC causes the time of an event to be associated not with that event, but with the following event at the HRC front end, which most likely is a background particle event rejected by the anti-coincidence shield and not telemetered to the ground (see POG, §7.10; Tennant et al. 2001). As a result, most of the true event times are lost, and the HRC timing accuracy degrades from the planned $16 \mu\text{s}$ to the mean time between events at the HRC front end, typically about 4 ms.

To circumvent this problem, the HRC team worked out a special operating mode which employs the HRC-S instrument. This mode uses only the central segment of the HRC-S, with two outer segments disabled, which lowers the overall counting rate below the telemetry saturation limit, even with all on-board vetoes disabled. As a result, all events are telemetered and can be assigned correct times by shifting the time-tags in ground processing.

The pulsar was re-observed in this new mode on 2000 October 6 (19.6 ks effective exposure). We measured the source count rate of 152 ± 6 counts ks^{-1} using the same aperture as for the HRC-I data. To perform the timing analysis, we first extracted the “arrival times” (as given in Level 2 data file) of 2,795 events from a $1''$ -radius circle centered at the pulsar (93% of the total number of source events). Then, for each of the selected events, we found the time of the following event in the Level 1 data file (which, in addition to photon events, contains time-tagged particle events) and assigned this later time to the selected source event. These corrected times were converted to equivalent arrival times at the solar system barycenter (SSB) in the barycentric dynamical time (TDB) system with the `axBary` tool⁹ using the solar system ephemeris DE200 (Standish 1982).

To correct the TDB arrival times for the effect of the orbital Doppler shift (Taylor & Weisberg 1989) and extract the light

curve, we used the pulsar and binary orbit ephemerides given in Table 1. The values of Z_n^2 statistics (Buccheri et al. 1983) calculated with the X-ray arrival times at the radio ephemeris parameters are $Z_1^2 = 217$, $Z_2^2 = 258$, $Z_3^2 = 259$. The difference between the radio period and that corresponding to the Z_2^2 maximum, $\delta P = 3 \times 10^{-12}$ s (or $\delta F = \delta P / P^2 = 1 \times 10^{-7}$ Hz), is negligible for the timing analysis of the X-ray data collected in a 20 ks time span. Note that δP is much smaller than the 1σ uncertainty (given by the Bayesian method — see Zavlin et al. [2000] for details), 1×10^{-10} s, of the period found in the HRC-S data. The small value of δP and the large Z_n^2 values prove unambiguously that the new HRC-S timing mode is fully capable of detecting millisecond pulsations. (The largest Z_n^2 values achieved in the ROSAT observations of this pulsar are 117 and 125 for $n = 1$ and $n = 2$, respectively).

The upper panel of Figure 5 presents the extracted HRC-S (energy-integrated) pulse profile of PSR J0437–4715. Using the radio ephemeris given in Table 1 and radio observations at frequencies close to 1400 MHz, made using the Parkes Telescope and the Caltech correlator (cf. Sandhu et al. 1997), which were contemporaneous with the X-ray observations, we were able to find the relation between the radio and X-ray phases — $\phi = 0$ in this figure corresponds to the maximum of the radio peak observed at 1420 MHz, dedispersed to infinite frequency using the DM in Table 1. The epoch of $\phi = 0$ is 51 823.7311148130996 MJD [UTC at geocenter]. Using TEMPO¹⁰, we determined the phase offsets of the X-ray peaks for five sub-intervals within the 20-ks exposure. The corresponding time offsets vary from $-6 \mu\text{s}$ to $+37 \mu\text{s}$, with a mean value of $+16 \mu\text{s}$ (0.3% of the pulsar period), equal to the intrinsic HRC time resolution. Therefore, we conclude that the phases of the X-ray and radio pulses are virtually the same — their difference does not exceed the errors of the *Chandra* absolute time¹¹. It should be noted that this is the first determination of the absolute phase of X-ray pulsations of PSR J0437–4715 — errors in absolute timing of the ROSAT data were at a 1–2 ms level (see HMM96 and BT99 for discussion), preventing the absolute phase determination.

For comparison, we also show in Figure 5 the pulse profiles obtained from the ROSAT PSPC and HRI observations of 1994 (with phases chosen to approximately co-align the ROSAT peaks with *Chandra* peak). The pulsed fraction¹² of the HRC-S light curve is somewhat larger than those in the ROSAT data. Since the HRC-S is more sensitive at higher energies than the ROSAT detectors, this may indicate that f_p increases with E , as predicted by the hydrogen polar cap model. In addition, the pulse in the HRC-S light curve looks slightly narrower than the PSPC and HRI pulses. This also could be explained by the properties of the thermal radiation emitted from a hydrogen atmosphere — the radiation intensities are more beamed at higher E (Zavlin et al. 1996).

5. DISCUSSION

The *Chandra* observations of PSR J0437–4715 have allowed us to perform the spatial, timing and spectral analyses of the new data collected with high angular and spectral resolution in an extended energy range.

The principal new result of the ACIS observation is the measurement of the pulsar’s X-ray spectrum at higher energies, up to 7 keV. Among the formally acceptable fits of the combined ROSAT PSPC and *Chandra* ACIS spectra, only the broken PL model corresponds to a purely nonthermal pulsar radiation in the X-ray band. However, the break energy of about 1.1 keV is 5–6 orders of magnitude lower than those observed in other pulsars. Such a difference looks too large to be explained by a lower magnetic field in the radiating region — it would also require a lower break energy in the spectrum of radiating electrons/positrons, compared to ordinary pulsars. Moreover, extrapolation of the broken PL model to the optical B and V bands (assuming the same slope as in the X-ray range below 1.1 keV) predicts optical magnitudes, $m_B = 19.6 \pm 1.4$ and $m_V = 19.1 \pm 1.4$ (for extinction coefficients $A_B = 0.3$, $A_V = 0.2$ — Danziger, Baade, & della Valle 1993), much brighter than those detected from the white dwarf companion, $m_B = 22.1 \pm 0.1$ and $m_V = 20.9 \pm 0.1$ (Bailyn 1993; Danziger et al. 1993; Bell et al. 1993). Thus, we do not consider the broken PL model to be a plausible interpretation.

The alternative model involves *two components* of different origin — thermal and nonthermal. The nonthermal component originates in the pulsar magnetosphere¹³, whereas the thermal component is emitted from hot polar caps on the NS surface. Depending on assumption about the polar cap temperature distribution, one gets different relative contributions from these two components. In the model with uniformly heated polar caps, the nonthermal component described as a PL of photon index $\gamma = 2.7 - 2.9$ provides about 80% in the X-ray flux and dominates at energies below 0.6 keV and above 2.7 keV. However, this model encounters the same problems in the EUV and optical bands as the broken PL (the steeper slope of this PL component predicts even higher fluxes in the B and V bands).

If we assume a more plausible polar cap model with temperature decreasing outwards from the cap center, then the thermal component becomes dominant between 0.06 keV and 2.5 keV, providing some 75% of the X-ray flux, while the PL component of $\gamma = 1.6 - 2.5$ dominates outside this band. In addition to a more realistic temperature distribution, the latter model is well consistent with the EUVE data and yields estimates on the hydrogen column density in agreement with the indirect measurements. As this PL component is fainter than in the two other models, its extension to the optical falls below the observed radiation of the white dwarf companion for photon indices $\gamma < 1.9$. This allows us to predict that the PL component should be observable in the UV (particularly, far-UV) range where it is brighter than the Wien tail of the white dwarf spectrum, assuming there is no turnover of the nonthermal spectrum between the UV and soft-X-ray energies. On the other side of the X-ray band, extrapolation of the PL component to the gamma-ray energies above 100 MeV predicts a pho-

¹⁰TEMPO is a program for the analysis of pulsar timing data maintained and distributed by Princeton University and the Australia Telescope National Facility. It is available at <http://www.atnf.csiro.au/research/pulsar/timing/tempo/>

¹¹The accuracy of the *Chandra* absolute time was estimated by Tennant et al. (2001) from the comparison of the *Chandra* HRC-I and *RXTE* timing of the Crab pulsar: $t_{\text{Chandra}} - t_{\text{RXTE}} = -200 \pm 100 \mu\text{s}$.

¹²Conventionally defined as the ratio of the number of counts above the minimum of the light curve to the total number of counts.

¹³Another source of unresolvable nonthermal radiation could be the shocked pulsar wind near the white dwarf companion (e.g., Arons & Tavani 1993). However, at the distance of $a_p = 1.5 \times 10^{11}$ cm from the pulsar (van Straten et al. 2001), the companion intercepts only a fraction $\sim 6 \times 10^{-4}$ of the wind (assuming the wind is approximately isotropic), too small to explain the observed nonthermal luminosity.

ton flux $f < 2 \times 10^{-8} \text{ s}^{-1} \text{ cm}^{-2}$ ($\gamma > 1.6$), below the upper limit, $f < 1.5 \times 10^{-7} \text{ s}^{-1} \text{ cm}^{-2}$, obtained from the *CGRO* EGRET observations (Fierro et al. 1995).

We emphasize that these models require the thermal radiation to be emitted from hydrogen (or helium) NS atmosphere. The high spectral resolution of the ACIS data rules out an atmosphere comprised of heavier chemical elements.

The HRC-S observation of PSR J0437–4715 has demonstrated the *Chandra* timing capability at a millisecond level. The HRC-S pulse profile looks narrower, and the pulsed fraction is somewhat higher, than those obtained in the earlier *ROSAT* and *EUVE* observations at lower energies, which could be explained by the properties of the thermal radiation from polar caps covered with a hydrogen or helium atmosphere. On the other hand, the shape of the profile is clearly asymmetric, with a longer rise and faster decay, which cannot be explained by a simple axisymmetric temperature distribution. Relativistic effects (particularly, the Doppler boost) should lead to a different asymmetry — a faster rise and longer trail (Braje & Romani 2000; Ford 2000). The analysis of HRC-S data demonstrates, for the first time, that the phase of the X-ray pulse virtually coincides with that of the radio pulse. If, as we suggest, the main contribution to the HRC-S band is due to the thermal polar cap radiation, and if the pulsar radio beam is directed along the magnetic axis, then the radio emission must be generated close to the NS surface — e.g., the time difference of < 0.1 ms between the X-ray and radio phases corresponds to a distance of < 30 km, much smaller than the light cylinder radius, $R_{lc} = 275$ km. Alternatively, if the radio emission is generated at a higher altitude, the combination of field-line sweepback and aberration must contrive to cancel the radial travel-time difference.

The *Chandra* observations show no sign of an X-ray PWN that could accompany the bow-shock revealed by the H_α observations. Three-sigma upper limits on the PWN brightness (in counts arcsec $^{-2}$) can be estimated as $3(b/A)^{1/2}$, where b is the background surface brightness ($b = 0.51$ and 0.28 counts arcsec $^{-2}$ for the ACIS-S and HRC-I images, respectively), and A is the PWN area (we will scale it as $A = 1000f_A$ arcsec 2 , assuming that a typical transverse size of the PWN somewhat exceeds the stand-off distance, $10''$, of the bow shock). For a power-law PWN spectrum with a photon index $\gamma = 1.5$ – 2 (similar to those observed from other PWNs), these upper limits correspond to the PWN intensities $I_{x,pwn} < (1.3$ – $1.8) \times 10^{-17} f_A^{-1/2}$ and $I_{x,pwn} < (3.6$ – $5.7) \times 10^{-17} f_A^{-1/2}$ erg cm $^{-2}$ s $^{-1}$ arcsec $^{-2}$, for the ACIS-S and HRC-I, respectively, in the 0.1–10 keV range. The corresponding upper limits on the PWN X-ray luminosity, $L_{x,pwn} \approx 4\pi d^2 A I_{x,pwn}$ are much smaller than the rotational energy loss rate, $\dot{E} = 3.8 \times 10^{33}$ erg s $^{-1}$ — e.g., $L_{x,pwn} < (3.0$ – $4.2) \times 10^{28} f_A^{1/2}$ erg s $^{-1}$ for the more sensitive ACIS-S limit.

The low upper limits on the PWN luminosity in X-rays

can be simply explained by a low magnetic field in the PWN region, expected for a particle-dominated pulsar wind. The shock in the relativistic pulsar wind should be located just interior to the observed H_α bow shock (Arons & Tavani 1993). When the wind electrons pass through the shock, their directions of motion become “randomized”, and their synchrotron radiation may result in an X-ray nebula, provided the electron energies and the magnetic field are high enough in the post-shock region. The pre-shock magnetic field can be estimated as $B_1 = [\dot{E}/(f_\Omega r_s^2 c)]^{1/2} [\sigma/(1+\sigma)]^{1/2} = 18 f_\Omega^{-1/2} [\sigma/(1+\sigma)]^{1/2} \mu\text{G}$, where $r_s \approx 2 \times 10^{16}$ cm is the stand-off distance corresponding to $10''$ at $d = 140$ pc, $f_\Omega = \Delta\Omega/(4\pi) \leq 1$ is the collimation factor of the wind, and the “magnetization parameter” σ is the ratio of the Poynting flux to the kinetic energy flux. The maximum value of the post-shock magnetic field, $B \simeq B_1 \simeq 18 f_\Omega^{-1/2} \mu\text{G}$, is obtained for $\sigma \gg 1$. However, according to Kennel & Coroniti (1984; KC84 hereafter), a significant fraction of the total energy flux upstream can be converted into (observable) synchrotron luminosity downstream only if $\sigma \lesssim 0.1$ (e.g., these authors estimate $\sigma \approx 0.003$ for the Crab pulsar). For $\sigma \ll 1$, the post-shock magnetic field is $B \simeq 3(1-4\sigma)B_1 \simeq 53 f_\Omega^{-1/2} \sigma^{1/2} (1-4.5\sigma) \mu\text{G}$ (e.g., from eqs. [4.8] and [4.11] of KC84, B increases from $3 \mu\text{G}$ to $12 \mu\text{G}$ when σ increases from 0.003 to 0.1, at $f_\Omega = 1$). Such low magnetic fields in the shocked wind strongly limit the maximum energy, $m_e c^2 \Gamma_{\max}$, of radiating electrons and, consequently, the maximum frequency ν_{\max} of the synchrotron radiation. Since the Larmor radius of most energetic electrons, $r_L = 1.7 \times 10^8 \Gamma_{\max} B_{-5}^{-1}$ cm, cannot exceed the shock radius r_s substantially, we obtain $\Gamma_{\max} < 10^8 f_s B_{-5}$, $h\nu_{\max} \sim (heB/4\pi m_e c) \Gamma_{\max}^2 < 0.6 f_s^2 B_{-5}^3$ keV, where $B_{-5} = B/(10 \mu\text{G})$, $f_s \equiv r_L/r_s \sim 1$. If, for instance, $B < 5 f_s^{-2/3} \mu\text{G}$ (i.e., $\sigma < 0.01 f_s^{-4/3}$ in the KC84 model), the synchrotron emission at the bow shock is not expected to be seen in X-rays.

Despite the superior quality of the *Chandra* data, which have allowed us to detect the hard tail of the pulsar’s spectrum and pinpoint the absolute phase of the X-ray pulse, there still remain some open problems. Although our analysis strongly favors the thermal+nonthermal interpretation, it is still unclear which of the two components dominates in the X-ray radiation of PSR J0437–4715. To establish the relative contributions of these components, energy-resolved timing and time-resolved spectral analysis are needed, which, hopefully, will be possible with the forthcoming *XMM-Newton* data.

We thank Leisa Townsley for the advise on the ACIS data reduction, Allyn Tennant for the discussion of the HRC timing issues, and Willem van Straten for providing the timing ephemeris given in Table 1. We also thank Vadim Burwitz for helping in preparation of the color image. This work was partially supported by NASA through grants NAG5-7017, NAG5-10865, and SAO GO0-1126X.

REFERENCES

- Arons, J. 1981, *ApJ*, 284, 1099
Arons, J., & Tavani, M. 1993, *ApJ*, 403, 249
Bailyn, C. D. 1993, *ApJ*, 411, L83
Bautz, M. W., et al. 1998, *Proc. SPIE*, 3444, 210
Becker, W., & Pavlov, G. G. 2001, in *The Century of Space Science*, ed. J. Bleeker, J. Geiss & M. Huber (Dordrecht: Kluwer), in press
Becker, W., & Trümper, J. 1993, *Nature*, 365, 528 (BT93)
Becker, W., & Trümper, J. 1999, *A&A*, 341, 803 (BT99)
Becker, W., Trümper, J. Lommen, A. E., & Backer, D. C. 2000, *ApJ*, 545, 1015
Bell, J. F., Bailes, M., & Bessell, M. S. 1993, *Nature*, 364, 603
Bell, J. F., Bailes, M., Manchester, R. N., Weisberg, J. M., & Lyne, A. G. 1995, *ApJ*, 440, L81
Beskin, V. S., Gurevich, A. F., & Istomin, Ya. N. 1993, *Physics of Pulsar Magnetosphere*, (Cambridge: Cambridge Univ. Press)
Braje, T. M., & Romani, R. W. 2000, *ApJ*, 531, 447
Buccheri, R., et al. 1983, *A&A*, 128, 245
Cheng, A. F., & Ruderman, M. A. 1980, *ApJ*, 235, 576
Danziger, I. J., Baade, D., & della Valle, M. 1993, *A&A*, 276, 382

- Fierro, J. M., et al. 1995, ApJ, 447, 807
- Ford, E. C. 2000, ApJ, 535, L119
- Garmire, G. P., et al. 1992, AIAA Space Programs and Technologies Conf., Paper 92-1473 (Washington, DC: AIAA)
- Halpern, J. P., & Marshall, H. L. 1996, ApJ, 464, 760
- Halpern, J. P., Martin, C., & Marshall, H. L. 1996, ApJ, 462, 908 (HMM96)
- Johnston, S., et al. 1993, Nature, 361, 613
- Kawai, N., Tamura, K., & Saito, Y. 1998, Adv. Space Res., 21, 213
- Kennel, C. F., & Coroniti, F. V. 1984, ApJ, 283, 107
- Michel, F. S. 1991, Theory of Neutron Star Magnetospheres, (Chicago: Univ. of Chicago Press)
- Mineo, T., et al. 2000, A&A, 355, 1053
- Murray, S. S., et al. 1997, Proc. SPIE, 3114, 11
- Navarro, J., Manchester, R. N., Sandhu, J. S., Kulkarni, S. R., & Bailes, M. 1997, ApJ, 486, 1019
- Pavlov, G. G., & Zavlin, V. E. 1997, ApJ, 490, L91
- Pavlov, G. G., & Zavlin, V. E. 2000, in Highly Energetic Physical Processes and Mechanisms for Emission from Astrophysical Plasmas, IAU Symp. 195, ed. P. C. H. Martens, S. Tsuruta & M. A. Weber, p.103
- Pavlov, G. G., Zavlin, V. E., Sanwal, D., Burwitz, V., & Garmire, G. P. 2001, ApJ, 552, L129
- Rajagopal, M., & Romani, R. W. 1996, ApJ, 461, 327
- Saito, Y., Kawai, N., Kamae, T., Shibata, S., Dotani, T., & Kulkarni, S. R. 1997, ApJ, 477, L37
- Sandhu, J. S., Bailes, M., Manchester, R. N., Navarro, J., Kulkarni, S. R., & Anderson, S. B. 1997, ApJ, 478, L95
- Sanwal, D., Pavlov, G. G., Zavlin, V. E., Teter, M., & Tsuruta, S. 2000, BAAS, 32, 1241
- Standish, E. M. 1982, A&A, 114, 297
- Takahashi, M., et al. 2001, ApJ, 554, 316
- Taylor, J. H., Manchester, R. N., & Lyne, A. G. 1993, ApJS, 89, 189
- Taylor, J. H., & Weisberg, J. M. 1989, ApJ, 345, 434
- Tennant, A., et al. 2001, ApJ, 554, L173
- Tsuruta, S. 1998, Phys. Rep., 292, 1
- van Straten, W., Bailes, M., Britton, M., Kulkarni, S. R., Anderson, S. B., Manchester, R. N., & Sarkissian, J. 2001, Nature, 412, 158
- Zavlin, V. E., & Pavlov, G. G. 1998, A&A, 329, 583 (ZP98)
- Zavlin, V. E., Shibanov, Yu. A., & Pavlov, G. G. 1995, Astron. Let., 21, 149
- Zavlin, V. E., Pavlov, G. G., & Shibanov, Yu. A. 1996, A&A, 315, 141
- Zavlin, V. E., Pavlov, G. G., Sanwal, D., & Trümper, J. 2000, 540, L25

TABLE 1
Ephemeris parameters for the binary pulsar J0437–4715^a

Parameter	Value
R.A. (J2000).....	04 ^h 37 ^m 15 ^s .78651377
Dec. (J2000).....	−47°15′ 8″.46158135
μ_α (mas/yr).....	121.4565
μ_δ (mas/yr).....	−71.4494
Parallax (mas).....	6.9830
F (Hz).....	173.68794899909872242
\dot{F} (10^{-15} s ^{−2}).....	−1.728325769909
\ddot{F} (10^{-30} s ^{−3}).....	132.1214177
Epoch of period and position (MJD).....	51,194.0
DM (cm ^{−3} pc).....	2.64690
Binary period, P_b (days).....	5.741044490290
$x = a_p \sin i$ (lt-s) ^b	3.366693427
Eccentricity, e	0.000019193
Longitude of periastron, ω (deg).....	1.848063
Epoch of periastron (MJD).....	51,194.634254236
\dot{x} (10^{-12} lt-s s ^{−1}).....	0.078270
\dot{P}_b (10^{-12} s s ^{−1}).....	3.397

^aBased on radio observations made using the Parkes 64-m telescope of the Australia Telescope National Facility (van Straten et al. 2001)

^bProjected semi-major axis of the pulsar’s orbit

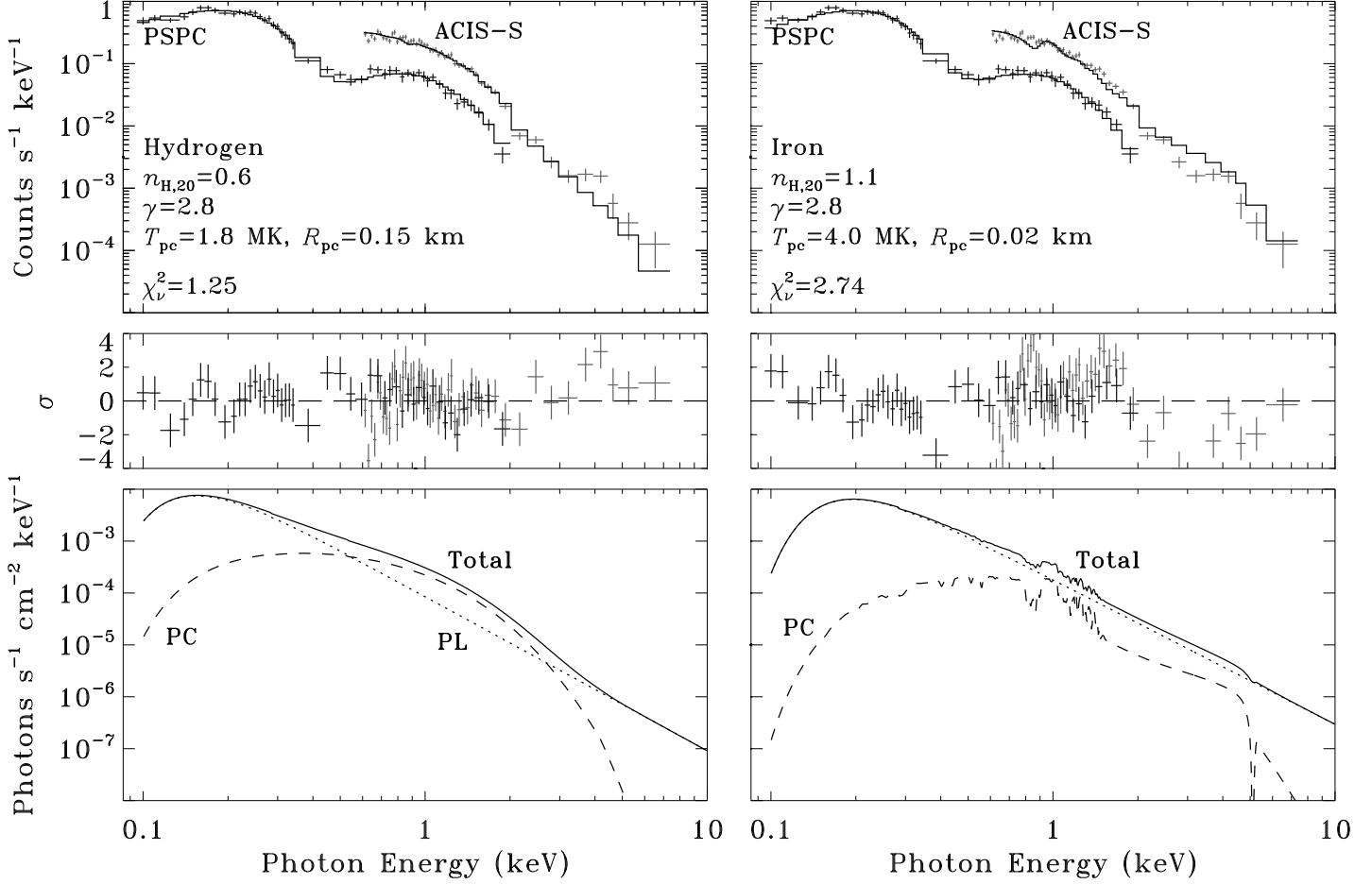


FIG. 1.— Power-law plus one-temperature polar cap model fits to the *ROSAT* and *Chandra* spectra. The left and right panels correspond to polar caps covered with hydrogen and iron atmospheres, respectively.

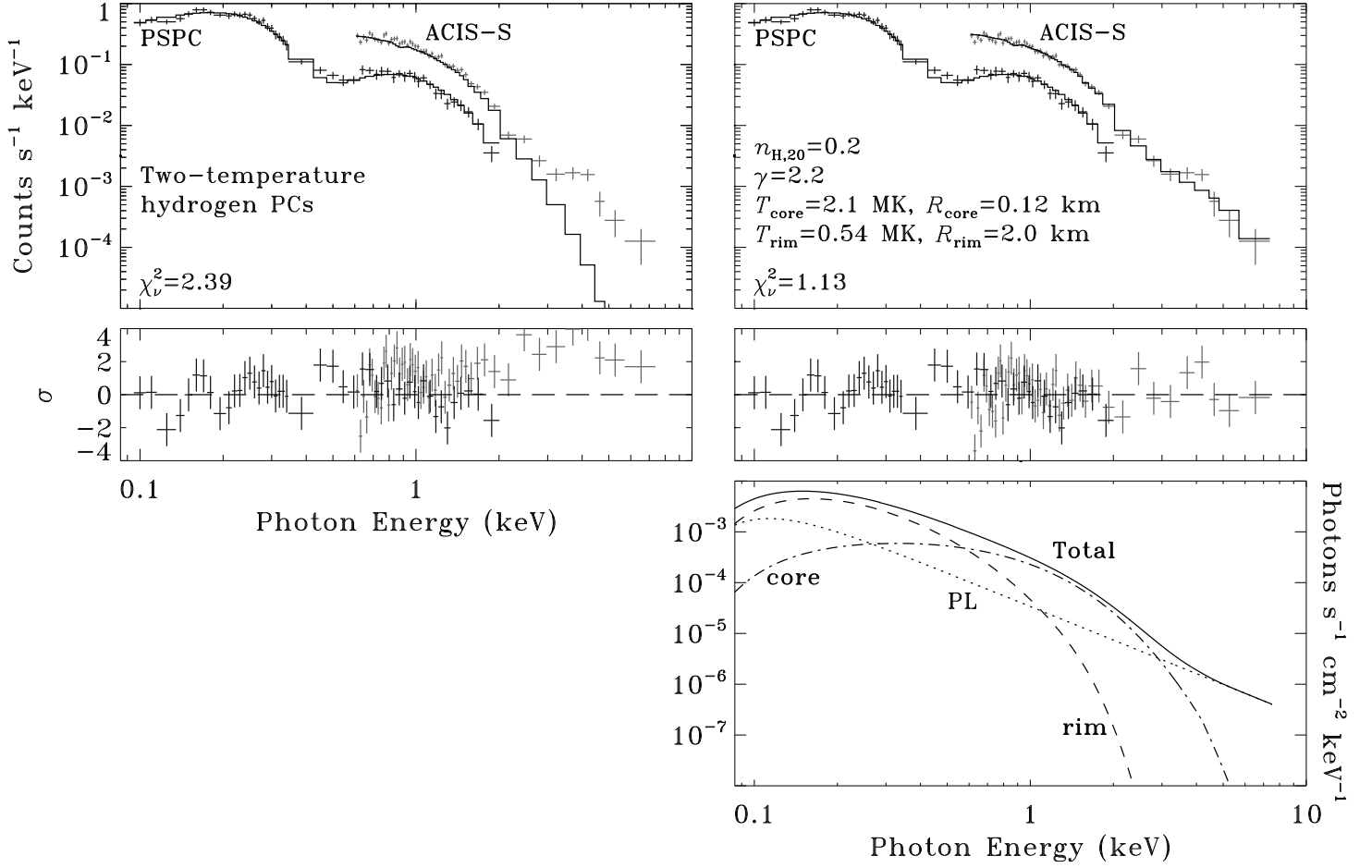


FIG. 2.— Two-temperature polar cap model fits with and without the power-law component (right and left panels, respectively).

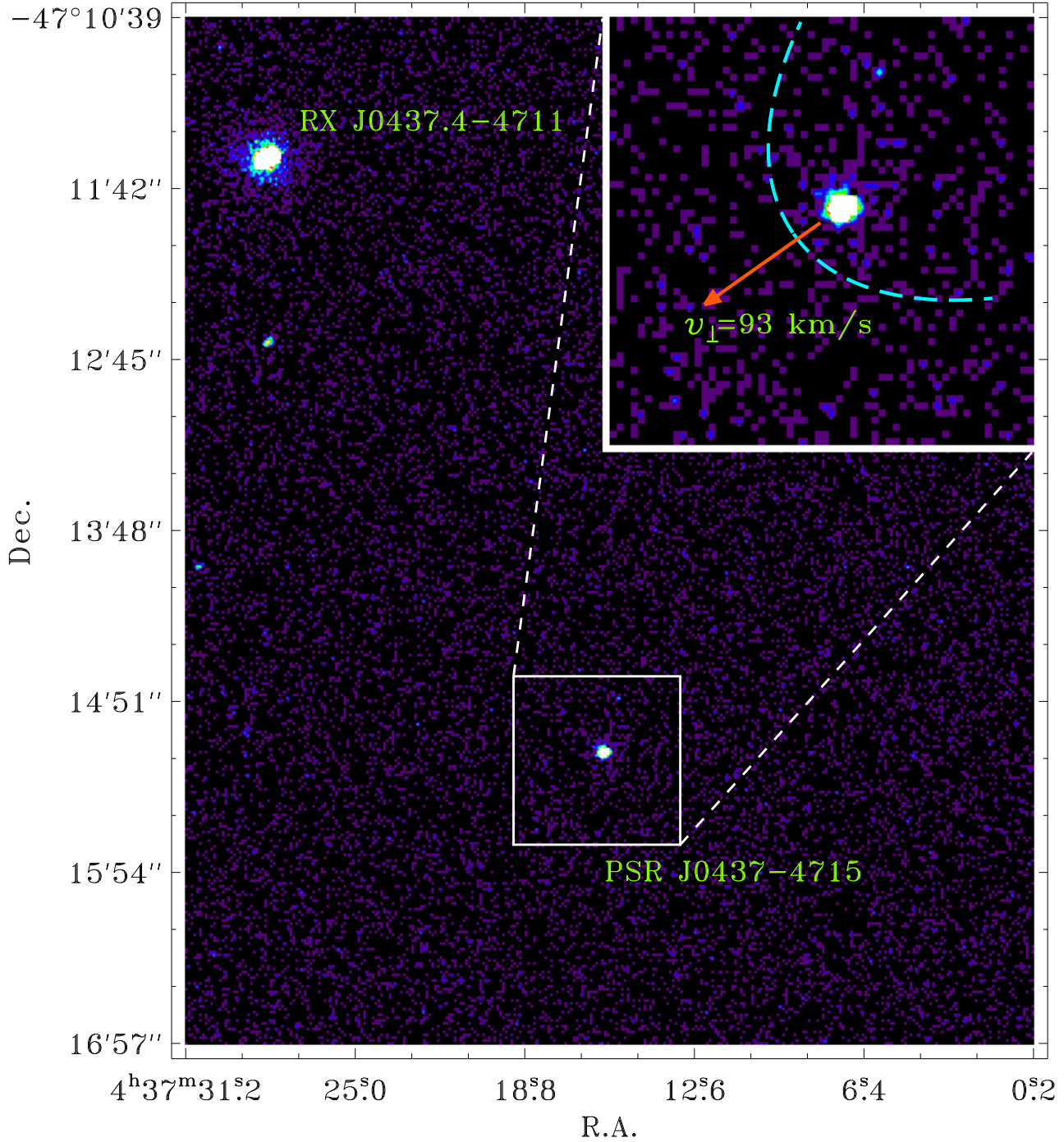


FIG. 3.— 5.2 × 6.3 region of the HRC-I image. The bright source in the upper-left corner is an AGN (Halpern & Marshall 1996). The inset in the upper-right corner shows a zoomed 63'' × 63'' field around the pulsar. The dashed curve marks the leading edge of the H_α bow-shock. The arrow shows the direction of the pulsar's proper motion, with the transverse velocity v_{\perp} .

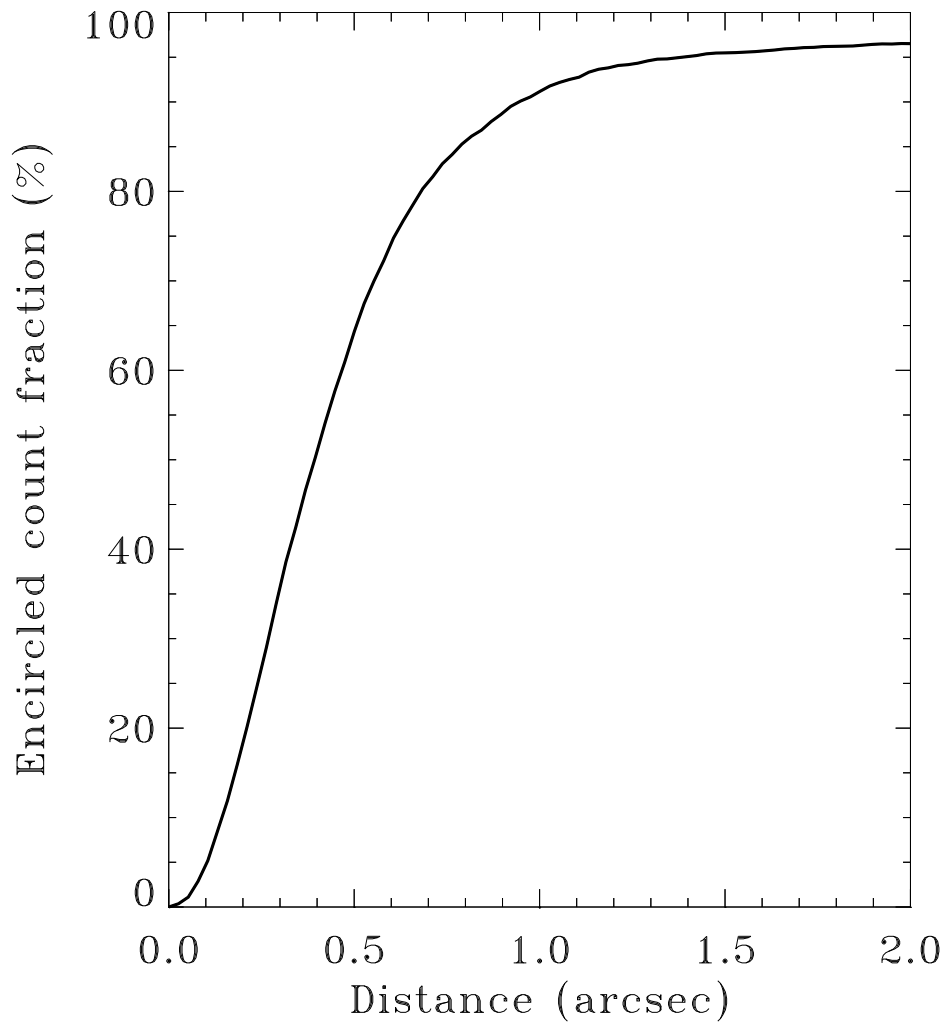


FIG. 4.— Radial distribution of encircled fraction of pulsar counts in the HRC-I data.

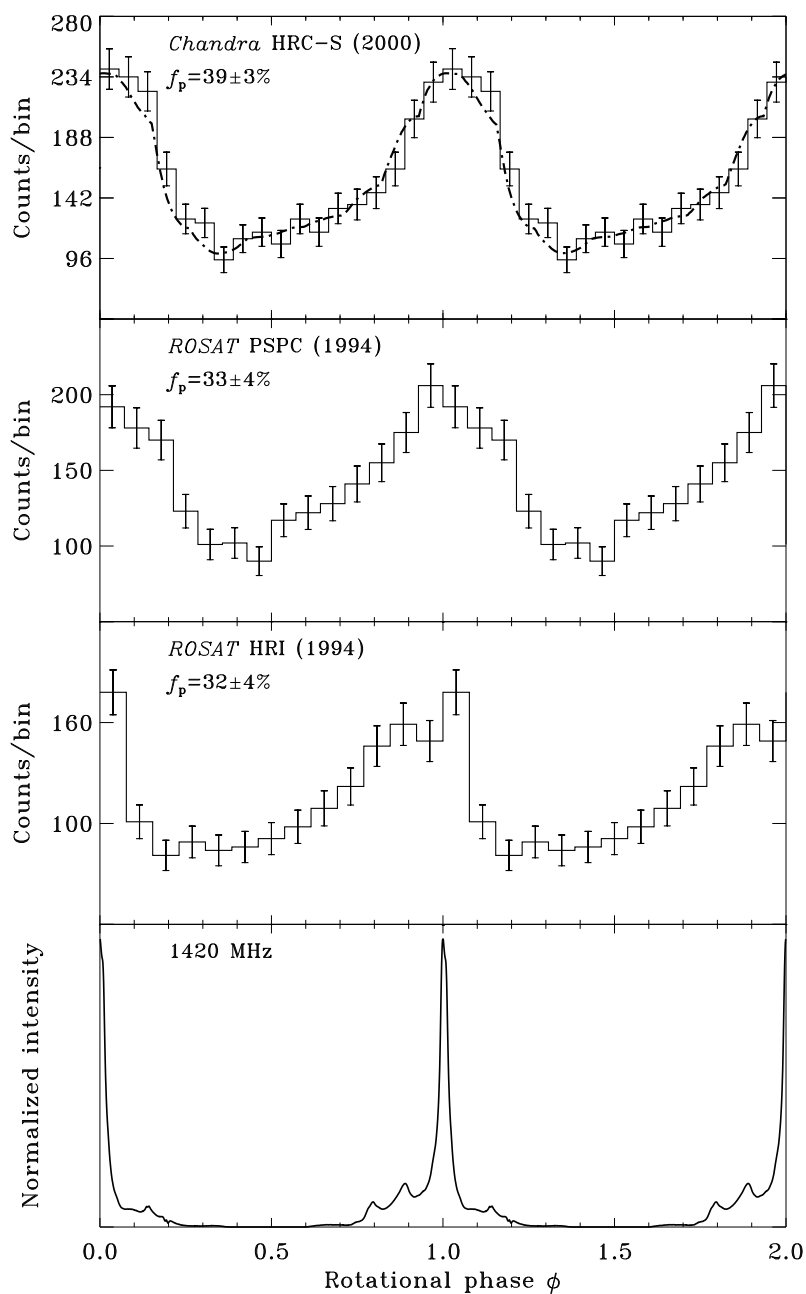


FIG. 5.— Pulse profiles of PSR J0437–4715 from the *Chandra*, *ROSAT*, and radio observations. The smooth light curve in the upper panel is obtained by averaging of the 20-bin profile over the starting phase. The zero phase corresponds to the peak of the radio pulse shown in the lower panel which is the summed profile from the 1400 MHz radio observations made with the Caltech correlator at Parkes. The absolute phases of the *ROSAT* pulses were not measured; we chose the phases to approximately co-align these pulses with the *Chandra* pulse.